



Contents lists available at ScienceDirect

Journal of Colloid and Interface Science

journal homepage: www.elsevier.com/locate/jcis

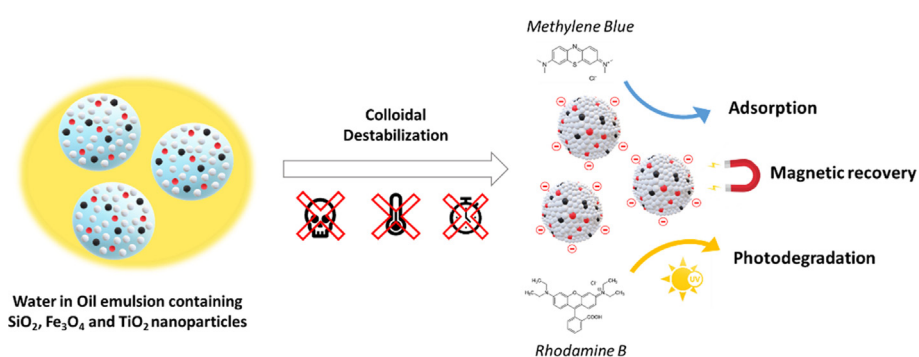
Regular Article

Self-assembly of $\text{TiO}_2/\text{Fe}_3\text{O}_4/\text{SiO}_2$ microbeads: A green approach to produce magnetic photocatalystsDavid F.F. Brossault^{a,b}, Thomas M. McCoy^{a,b}, Alexander F. Routh^{a,b,*}^a BP Institute, University of Cambridge, Madingley Rise, Cambridge CB3 0EZ, United Kingdom^b Department of Chemical Engineering and Biotechnology, University of Cambridge, Philippa Fawcett Dr, Cambridge CB3 0AS, United Kingdom

HIGHLIGHTS

- $\text{TiO}_2/\text{Fe}_3\text{O}_4/\text{SiO}_2$ microbead preparation: aggregation of nanoparticles in emulsion.
- Environmentally friendly: room temperature and non-hazardous chemicals.
- Simple: commercial nanoparticles and basic lab equipment.
- Fast: less than one hour for final product.
- Microbead properties: photocatalytic, magnetic and adsorbent.

GRAPHICAL ABSTRACT



ARTICLE INFO

Article history:

Received 10 September 2020

Revised 30 September 2020

Accepted 1 October 2020

Available online 13 October 2020

Keywords:

Green chemistry
Magnetic photocatalysts
Emulsion
Nanoparticles
Hetero-coagulation
Water treatment

ABSTRACT

Hypothesis: A green approach for producing magnetic photocatalysts via direct agglomeration of commercial nanoparticles in emulsion is shown. Aggregation is attributed to charge screening by salt addition which reduces stabilising repulsive forces between particles, and different nanoparticles (TiO_2 , Fe_3O_4 and SiO_2) serve to imbue the final agglomerates with desired adsorption, photodegradation and magnetic properties.

Experiment: Titania doped magnetic silica microbeads ($\text{TiO}_2/\text{Fe}_3\text{O}_4/\text{SiO}_2$) were produced at room temperature by CaCl_2 -induced aggregation of nanoparticles in a reverse emulsion template. The beads were characterized using optical microscopy, SEM, STEM, EDX and zeta potential measurements. The adsorption and photocatalytic properties of the system as well as its reusability were investigated using Rhodamine B and Methylene Blue as model pollutants.

Results: Magnetically responsive beads approximately 3–9 μm in diameter incorporating SiO_2 , TiO_2 and Fe_3O_4 nanoparticles were produced. Adsorption and photodegradation properties of the beads were confirmed by bleaching solutions of Rhodamine B, Methylene Blue as well as mixtures of both dyes. Reusability of the beads after magnetic separation was demonstrated, exhibiting a dye removal efficiency greater than 93% per cycle for three consecutive cycles of UV-light irradiation. This method is simpler than conventional sol-gel methods and offers a green and easy to implement approach for producing structured functional materials.

© 2020 Elsevier Inc. All rights reserved.

* Corresponding author at: Department of Chemical Engineering and Biotechnology, University of Cambridge, Philippa Fawcett Dr, Cambridge CB3 0AS, United Kingdom.
E-mail addresses: dffb2@cam.ac.uk (D.F.F. Brossault), tm657@cam.ac.uk (T.M. McCoy), af10@cam.ac.uk (A.F. Routh).

1. Introduction

Magnetic photocatalysts are composite systems comprising a semiconductor, which generates highly reactive oxidizing species under light excitation, and a magnetic material that enables enhanced recovery capabilities [1–6]. This dual nature has rendered such systems as promising and effective candidates for heterogeneous catalysis with applications in both organic synthesis and air/water remediation [2,7,8]. The combination of photocatalytic and magnetic properties was proven to be especially interesting for water treatment applications, enabling the degradation of diverse organic compounds such as pharmaceutical ingredients [9–12], agrochemicals [13,14], synthetic dyes [3–5,13] and microbial contaminants [15] under light irradiation. Use of an external magnetic field then allows an easy post-treatment recovery of the particles [1–3,6,13]. Such features circumvent the necessity of high treatment cost, limited targets and secondary waste pollution derived from conventional chemical, physical and biological water treatment techniques [16,17].

Various combinations of magnetic materials (Fe_3O_4 , $\gamma\text{-Fe}_2\text{O}_3$, CoFe_2O_4 , NiFe_2O_4 , ...) and semiconductors (TiO_2 , ZnO , WO_3 , CdS , SnO_2 , BiOCl ...) have been reported over recent decades [3,6,13,18–21]. Among those potential semiconductors, TiO_2 appeared as one of the leading candidates due to being efficient, minimally toxic, chemically stable and offering a high surface area [16,18]. Fe_3O_4 has been preferred to other magnetic materials due to its ease of synthesis, high magnetism, low cost and low toxicity [5,6,13]. Various core shell systems combining TiO_2 and Fe_3O_4 have been reported in literature over the past few years [5,10,22–35]. Preparation of these systems is traditionally composed of 3 to 4 distinct steps [5]. The first step involves synthesis of Fe_3O_4 nanoparticles by techniques such as co-precipitation of ferric and ferrous salts [10,23,24,29], solvothermal approaches [27,28,30,31,33] or use of commercially acquired Fe_3O_4 nanoparticles [32,34]. The second stage usually consists of coating the magnetic core with an intermediate metal oxide layer. Silica is usually added during this stage via a sol–gel approach using Tetraethyl orthosilicate (TEOS) and ammonia [10,22,28,32,34]. This intermediate coating aims to protect the titania layer added subsequently from a loss of photoactivity caused by direct contact with the magnetic core [4,5]. However, some procedures opt to omit this step, directly producing magnetite-titania binary composites [26,27,29,30,33,35]. The third step then involves coating with titania. For this, sol–gel approaches [19,23,34] or solvothermal methods [24,25,27,28,31,33] using titanium alkoxide precursors (TBOT, TTIP, TEOT ...) have been reported. This step is often followed by a heat treatment carried out at temperatures greater than 400 °C to transform the amorphous titania layer into its crystalline anatase phase which offers photocatalytic properties.

Conventional sol–gel and solvothermal approaches have successfully been used to prepare titania-based magnetic photocatalysts. However, these methods have three major limitations: they are often time-consuming due to multiple hour-long steps, they require high temperatures and toxic chemicals, and the need for sequential synthesis steps and heat treatment makes their implementation challenging and costly on a large scale. To overcome these limitations, alternative production methods such as hetero-coagulation of nanoparticles have been reported [36–38]. This approach is based on the interactions derived from particle surface charges such as electrostatic attraction and repulsion. Dewi *et al.* reported the possibility of adsorbing TiO_2 nanoparticles on $\text{Fe}_3\text{O}_4/\text{SiO}_2$ composites by adjusting the solution pH. At pH 5, TiO_2 and $\text{Fe}_3\text{O}_4/\text{SiO}_2$ nanoparticles were oppositely charged, resulting in fast agglomeration after mixing [36]. Costa *et al.* reported preparation of magnetic photocatalysts using exclusively commercial nanoparti-

cles. For this, TiO_2 and SiO_2 nanoparticles were subsequently adsorbed on Fe_3O_4 nanoparticles using a layer-by-layer approach. This method appears promising, as it has the advantages of safety and ease of preparation. However, the layer-by-layer approach is time-consuming, requiring 12 and 24 h consecutively for the adsorption of SiO_2 and TiO_2 [37]. Therefore, optimization of the hetero-coagulation process to improve efficiency is necessary.

Previously we have reported a green approach to produce tunable magnetic silica microbeads ($\text{Fe}_3\text{O}_4/\text{SiO}_2$) via colloidal destabilization of commercial nanoparticles in reverse emulsion phases [39]. This process differed from formerly reported approaches where magnetically responsive systems were produced using sol–gel methods [40–42] or polymerization in emulsions [43,44]. In our process, Fe_3O_4 and SiO_2 nanoparticles were dispersed in an aqueous solution before preparation of a water-in-oil emulsion. At pH 9, both nanoparticles were negatively charged and therefore electrostatically stable. Addition of CaCl_2 to the mixture resulted in screening of surface charges, facilitating an irreversible agglomeration of the nanoparticles contained within the aqueous droplets. The use of an emulsion as a structural template enabled precise control of both shape and diameter of the beads produced. This approach was found to be fast (less than 1 h), facile and environmentally friendly, due to the absence of toxic chemicals or high temperatures. This paper demonstrates and investigates the production of functional colloidal microbeads of $\text{TiO}_2/\text{Fe}_3\text{O}_4/\text{SiO}_2$ using a similar hetero-coagulation approach. These beads are shown to exhibit selective adsorption, photodegradation and magnetic properties. The potential for this system in water treatment applications is investigated with removal of two model synthetic dyes from water: Rhodamine B and Methylene Blue.

2. Experimental section

2.1. Materials

Sunflower oil (Sainsbury's) containing various amounts of Sorbitan monooleate (Span 80, Sigma-Aldrich) was used as the oil phase. The aqueous phase was composed of commercially available silicon dioxide (SiO_2 , Ludox HS40, 40 wt% dispersion in water, diameter 23 nm, Sigma Aldrich), titanium dioxide (TiO_2 , dry powder, diameter 21 nm, 99.5%, Sigma Aldrich) and iron oxide (Fe_3O_4 , dry powder, diameter 50–100 nm, 97%, Alfa Aesar) nanoparticles dispersed in a polyoxyethylenesorbitan monolaurate solution (Tween 20, Aqueous organics). Calcium chloride ($\text{CaCl}_2 \cdot 2\text{H}_2\text{O}$, Sigma-Aldrich) and Absolute ethanol (Fisher Scientific) were used during the formation and cleaning of beads. Rhodamine B (95%, Sigma Aldrich) and Methylene Blue (Lab grade, Riedel-de Haen) were chosen as model dyes for photodegradation experiments. All chemicals were used as received without additional purification.

2.2. Preparation of SiO_2 , $\text{Fe}_3\text{O}_4/\text{SiO}_2$ and $\text{TiO}_2/\text{Fe}_3\text{O}_4/\text{SiO}_2$ beads

SiO_2 beads, $\text{Fe}_3\text{O}_4/\text{SiO}_2$ beads and $\text{TiO}_2/\text{Fe}_3\text{O}_4/\text{SiO}_2$ beads, were produced via salt-induced destabilization of nanoparticles in reverse emulsion droplets, as shown in Fig. 1. The aqueous phase was prepared by mixing SiO_2 (30 wt%), Fe_3O_4 (0 or 5 wt%), TiO_2 (0 or 5 wt%) and Tween 20 (1 wt%) for 60 s with an ultrasonic homogenizer (Sonic Dismembrator FB-120, Fisher Scientific). At the experimental pH, measured between 9 and 10, all nanoparticles were negatively charged. The oil phase was prepared via addition of 0, 0.5, 1, 1.5 or 2 wt% of Span 80 in sunflower oil. The emulsion was then prepared via dropwise addition of 1 mL of the aqueous phase to 99 mL of oil phase stirred at 5000 RPM using a

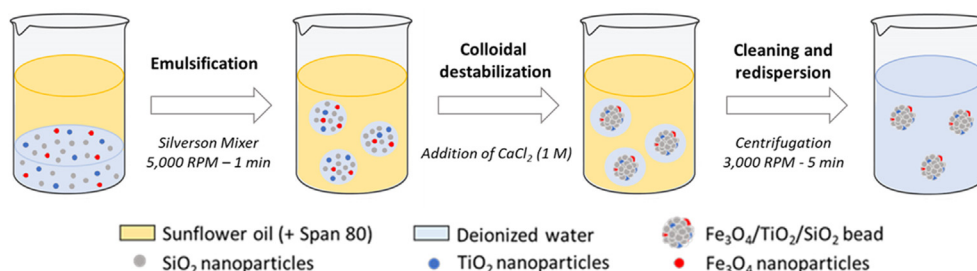


Fig. 1. Stepwise preparation method of $\text{TiO}_2/\text{Fe}_3\text{O}_4/\text{SiO}_2$ beads.

Silverson mixer (model SL2). After complete addition of the aqueous phase, the mixture was left to stir for 1 min at 5000 RPM. The stirring speed was then decreased to 3000 RPM and 1 mL of CaCl_2 solution (1 mol L^{-1}) was added dropwise. The mixture was then separated into three tubes and centrifuged at 3000 RPM for 5 min using a Multifuge 1S-R (Heraeus). The oil phase was removed by decantation, and the particles were redispersed in 10 mL of absolute ethanol before undergoing a second centrifugation cycle. This was repeated a second time before finally redispersing the beads in 5 mL of deionized water.

2.3. Characterization methods

The size distribution, chemical composition and morphology of the beads were assessed using optical and electron microscopy. Optical microscopy images were obtained using a Leica DME microscope equipped with $10\times$ and $63\times$ magnification lenses. Scanning Electron Microscopy (SEM) images were obtained using a Tescan Mira3 FEG-SEM microscope (acceleration voltage of 5 kV). This setup was also used to confirm the incorporation of metal oxides to the structure via Energy Dispersive X-ray spectroscopy (EDX, acceleration voltage of 30 kV). Scanning transmission electron microscopy (STEM) images were obtained using a Talos F200X G2 from Thermo Scientific equipped with a Ceta 16 M camera at an acceleration voltage of 200 kV. All images were processed using ImageJ software (imagej.net), analysing 250 randomly chosen beads to determine their average diameter and polydispersity.

Two vials containing 250 μL of solution were dried in an oven at 120°C for 4 h to determine the final concentration of beads in solution as well as to estimate the preparation yield. Zeta potentials were measured on a Brookhaven Nanobrook Omni by phase-analysis light scattering (PALS). Samples were analysed in 1 cm pathlength polystyrene cuvettes using a palladium PALS electrode. Quoted values are an average of three measurements each consisting of 25 sinusoidal phase cycles at 25°C .

The beads' magnetic response was assessed by observing their separation from solution under an external magnetic field. For this, a 5 mL solution was exposed to a magnetic field generated by a Rare-earth neodymium magnet (NiCuNi, $20\times 20\text{mm}$, E-magnets UK).

2.4. Photodegradation experiments

For removal of Rhodamine B and Methylene Blue from solution, 20, 40 or 60 mg of beads were added to 50 mL of dye solution. The solutions were then exposed to UV-light (36 W, Light excitation: 365 nm). 5 mL of solution was then collected after 0, 15, 30, 45, 60 and 90 min and centrifuged at 10,000 RPM for 5 min. Absorbance by the supernatant was measured using a UV-visible spectrophotometer (Cary 60, Agilent technologies). For Methylene Blue solutions, absorbances were measured at a fixed wavelength

of 665 nm, in 1 cm pathlength polystyrene cuvettes. For Rhodamine B solutions, the absorption maximum was observed to shift and therefore was not at a fixed value. The reported absorption values correspond to the maximum in the absorption spectra. The beads and supernatant liquid were then reinjected into the solution for measuring at subsequent time intervals.

2.4.1. Simple degradation

Degradation of 1 and 10 mg L^{-1} dye solutions were investigated in the presence of 20 mg of SiO_2 , $\text{Fe}_3\text{O}_4/\text{SiO}_2$ and $\text{TiO}_2/\text{Fe}_3\text{O}_4/\text{SiO}_2$ beads under both visible and UV-light. Results were compared to absorbance of the pure dye solution, and dye in the presence of 2.5 mg of TiO_2 nanoparticles. This amount corresponds to the quantity of TiO_2 in the bead structure.

2.4.2. Effect of bead porosity and bead load

10 mg L^{-1} Rhodamine B solutions were degraded in the presence of 20 mg of $\text{TiO}_2/\text{Fe}_3\text{O}_4/\text{SiO}_2$ beads prepared with 0, 0.5, 1, 1.5 and 2 wt% Span 80, and in the presence of 40 and 60 mg of $\text{TiO}_2/\text{Fe}_3\text{O}_4/\text{SiO}_2$ beads prepared with 0.5 wt% Span 80.

2.4.3. Recycling tests

10 mg L^{-1} Rhodamine B and Methylene Blue solutions were degraded in the presence of 60 mg of $\text{TiO}_2/\text{Fe}_3\text{O}_4/\text{SiO}_2$ beads prepared with 0.5 wt% Span 80. After 90 min of UV exposure, the beads were recovered using a magnet and redispersed in fresh dye solution. This step was repeated three times, and results obtained were compared to the extent of degradation in the presence of 7.5 mg of TiO_2 nanoparticles.

2.4.4. Degradation of Rhodamine B / Methylene Blue mixtures

Rhodamine B / Methylene Blue mixtures containing either 1 or 5 mg L^{-1} of each dye were degraded in the presence of 60 mg of $\text{TiO}_2/\text{Fe}_3\text{O}_4/\text{SiO}_2$ beads prepared with 0.5 wt% Span 80. The beads' photodegradation efficiency upon reuse was also investigated by repeat experiments with the same materials.

3. Results and discussion

3.1. Preparation and characterization of SiO_2 , $\text{Fe}_3\text{O}_4/\text{SiO}_2$ and $\text{TiO}_2/\text{Fe}_3\text{O}_4/\text{SiO}_2$ beads

SiO_2 , $\text{Fe}_3\text{O}_4/\text{SiO}_2$ and $\text{TiO}_2/\text{Fe}_3\text{O}_4/\text{SiO}_2$ beads were obtained after addition of calcium chloride to reverse emulsions containing dispersed metal oxide nanoparticles. The addition of salt results in a decrease of the electrostatic repulsion between nanoparticles dispersed in aqueous droplets. This colloidal destabilization enables irreversible agglomeration of nanoparticles, which organize into spherical beads due to the emulsion template.

SiO_2 and $\text{Fe}_3\text{O}_4/\text{SiO}_2$ beads were prepared for use as blanks in photodegradation experiments. The optical and electron microscopy images presented in Figs. S1 and S2, confirmed the produc-

tion of spherical beads with diameters of 1.8 ± 0.8 and 3.6 ± 1.4 μm . The incorporation of Fe_3O_4 nanoparticles was confirmed with optical microscopy and EDX analysis. The presence of large black spots in the optical microscopy images suggests clusters of iron oxide nanoparticles in the structure. This is likely to be due to the strong attractive forces between iron oxide nanoparticles, making their dispersion in the aqueous phase challenging. The presence of large Fe_3O_4 agglomerates explains the increase in diameter and polydispersity of the final beads as well as weaker structures, implied by the prevalence of broken $\text{Fe}_3\text{O}_4/\text{SiO}_2$ beads (Fig. S2B). However, despite these structural inhomogeneities, $\text{Fe}_3\text{O}_4/\text{SiO}_2$ beads can easily be recovered from solution using an external magnetic field, providing further confirmation of Fe_3O_4 being present in the beads. This is consistent with our previous findings [39].

Preparation of $\text{TiO}_2/\text{Fe}_3\text{O}_4/\text{SiO}_2$ beads in the absence of Span 80 resulted in a smooth, spherical structure of 4.1 ± 1.6 μm in diameter as shown in Fig. 2A–B. These beads were solid and of low macroporosity, as suggested by the homogeneous grey colour displayed in the STEM images (Fig. 2C). The appearance of both grey and black spots in the inner structure was attributed to higher electron density TiO_2 and Fe_3O_4 nanoparticles. This hypothesis was confirmed with detection of both iron and titanium using EDX analysis (Fig. 2D). The slight increase in diameter between $\text{Fe}_3\text{O}_4/\text{SiO}_2$ and $\text{TiO}_2/\text{Fe}_3\text{O}_4/\text{SiO}_2$ beads as well as the results displayed on EDX and STEM images suggested a more homogeneous

dispersion of TiO_2 in the silica structure compared to Fe_3O_4 . Rapid separation of $\text{TiO}_2/\text{Fe}_3\text{O}_4/\text{SiO}_2$ beads from solution was achieved

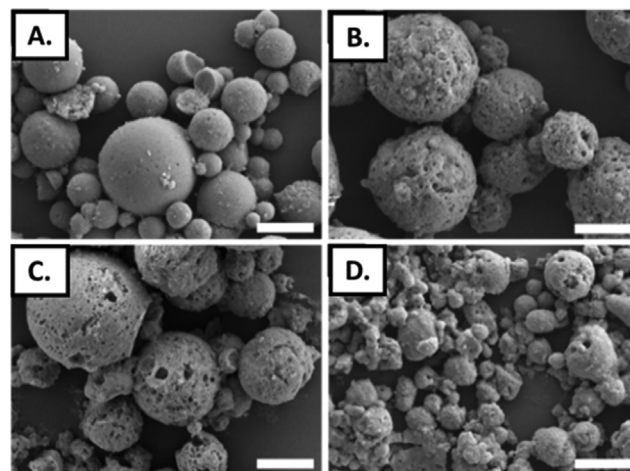


Fig. 3. SEM images of $\text{TiO}_2/\text{Fe}_3\text{O}_4/\text{SiO}_2$ beads produced with (A) 0.5 wt%, (B) 1.0 wt%, (C) 1.5 wt% or (D) 2.0 wt% Span 80 in the oil phase prior colloidal destabilization. Scale bars are equal to 5 μm .

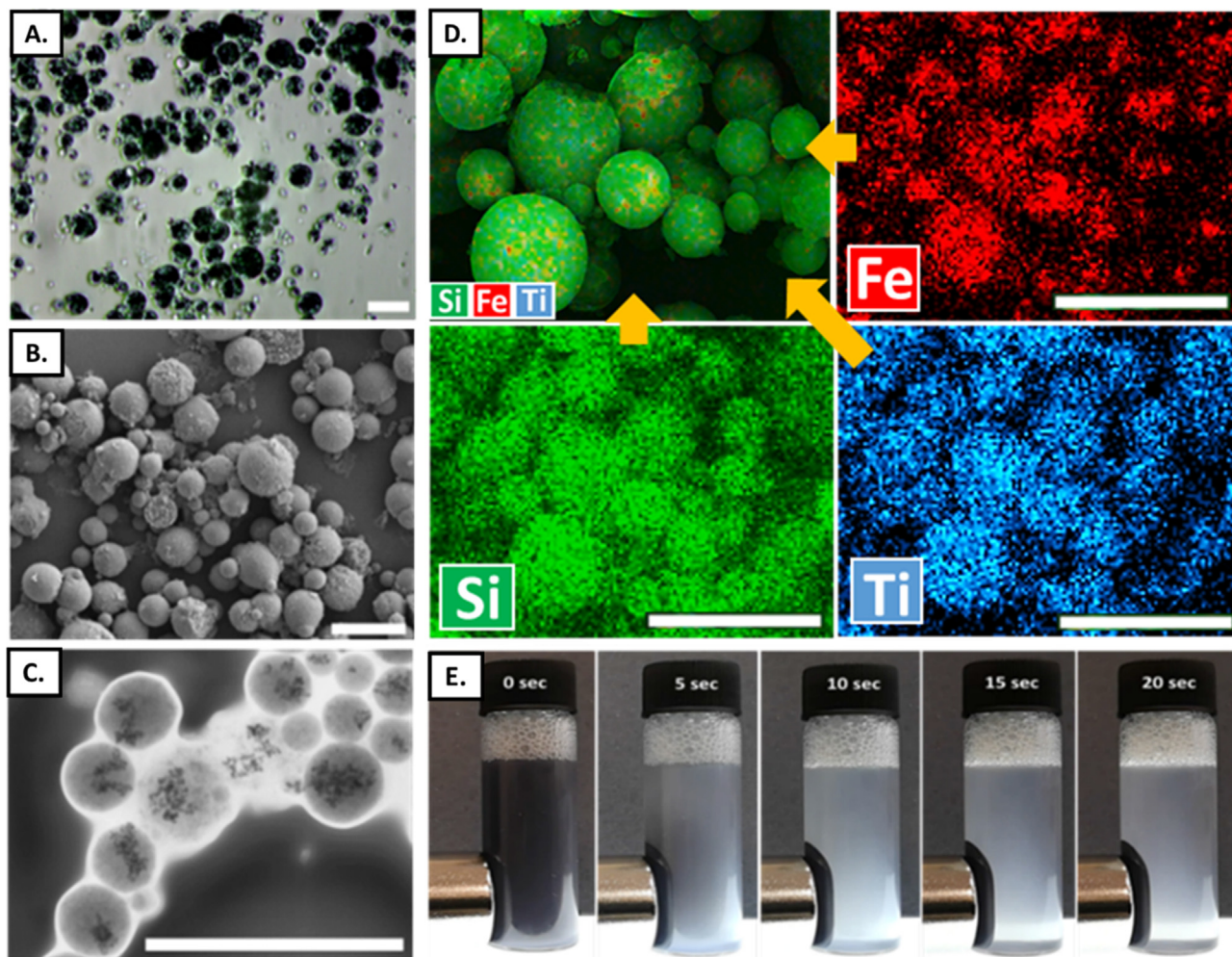


Fig. 2. Characterization of $\text{TiO}_2/\text{Fe}_3\text{O}_4/\text{SiO}_2$ beads prepared without Span 80: (A) Optical microscopy image; (B) SEM image; (C) STEM image and (D) EDX analysis images. Scale bars are equal to 10 μm . (E) Bead response to applied magnetic fields.

using a magnet (Fig. 2E), confirming magnetic responsiveness of the beads.

Addition of Span 80 in the oil phase resulted in modification of both the morphology and diameter of the $\text{TiO}_2/\text{Fe}_3\text{O}_4/\text{SiO}_2$ beads. SEM imaging shows an increase in roughness for samples prepared with higher concentrations of Span 80 (Fig. 3). It is believed that Span 80 adsorbs on the surface of silica nanoparticles, leading to incorporation of sunflower oil that serves to sterically distort particle aggregation during the salt addition step. Incorporated oil is then washed away during the cleaning process generating holes and cavities in the bead structure [39]. This approach enables one to produce porous materials without the use of a physical template, which would have to be subsequently removed using chemical or thermal methods. The impact of this porosity on the beads' photodegradation properties is investigated in the following sec-

tions. Analysis of SEM and optical microscopy images also highlights the significant impact of Span 80 concentration on the beads' size distribution. Results show that modifying the amount of Span 80 from 0 to 1.5 wt% yields larger beads, with the diameter increasing from 4.1 to 9.0 μm (Table 1). We hypothesise that this size increase may be caused by two phenomena. The first possibility is that surfactant induces destabilization of the W/O emulsion before coagulation. In the experimental conditions, some samples are produced at Span 80 concentrations above the surfactant critical micelle concentration (CMC), which has been estimated slightly below 1 wt% (22 mM) using UV-Visible spectrophotometry. Therefore, at higher concentrations of surfactant, Span 80 is organized in micelles, which could induce depletion interactions between water droplets and thus coalescence. The resulting droplets contain more nanoparticles leading to larger beads after col-

Table 1

Diameters, preparation yields, and electrophoretic mobilities of beads produced in various experimental conditions.

Beads composition	Diameter [μm] ^a	Mobility [$10^{-8}\cdot\text{m}^2\cdot\text{V}^{-1}\cdot\text{s}^{-1}$] ^b	Preparation Yield [%] ^c
SiO_2 (0% Span 80)	1.8 ± 0.8	-1.6 ± 0.1	80 ± 4
$\text{Fe}_3\text{O}_4/\text{SiO}_2$ (0% Span 80)	3.6 ± 1.4	-1.4 ± 0.2	72 ± 2
$\text{TiO}_2/\text{Fe}_3\text{O}_4/\text{SiO}_2$ (0% Span 80)	4.1 ± 1.6	-1.3 ± 0.1	64 ± 8
$\text{TiO}_2/\text{Fe}_3\text{O}_4/\text{SiO}_2$ (0.5% Span 80)	3.7 ± 1.4	-1.4 ± 0.1	68 ± 6
$\text{TiO}_2/\text{Fe}_3\text{O}_4/\text{SiO}_2$ (1.0% Span 80)	7.4 ± 2.7	-1.6 ± 0.2	72 ± 4
$\text{TiO}_2/\text{Fe}_3\text{O}_4/\text{SiO}_2$ (1.5% Span 80)	9.0 ± 3.1	-1.2 ± 0.0	81 ± 3
$\text{TiO}_2/\text{Fe}_3\text{O}_4/\text{SiO}_2$ (2% Span 80)	2.9 ± 1.1	-1.5 ± 0.1	60 ± 2

^a Based on 250 randomly chosen beads on SEM images.

^b Measurements carried out at pH 7.0.

^c Based on analysis of 2 batches per sample.

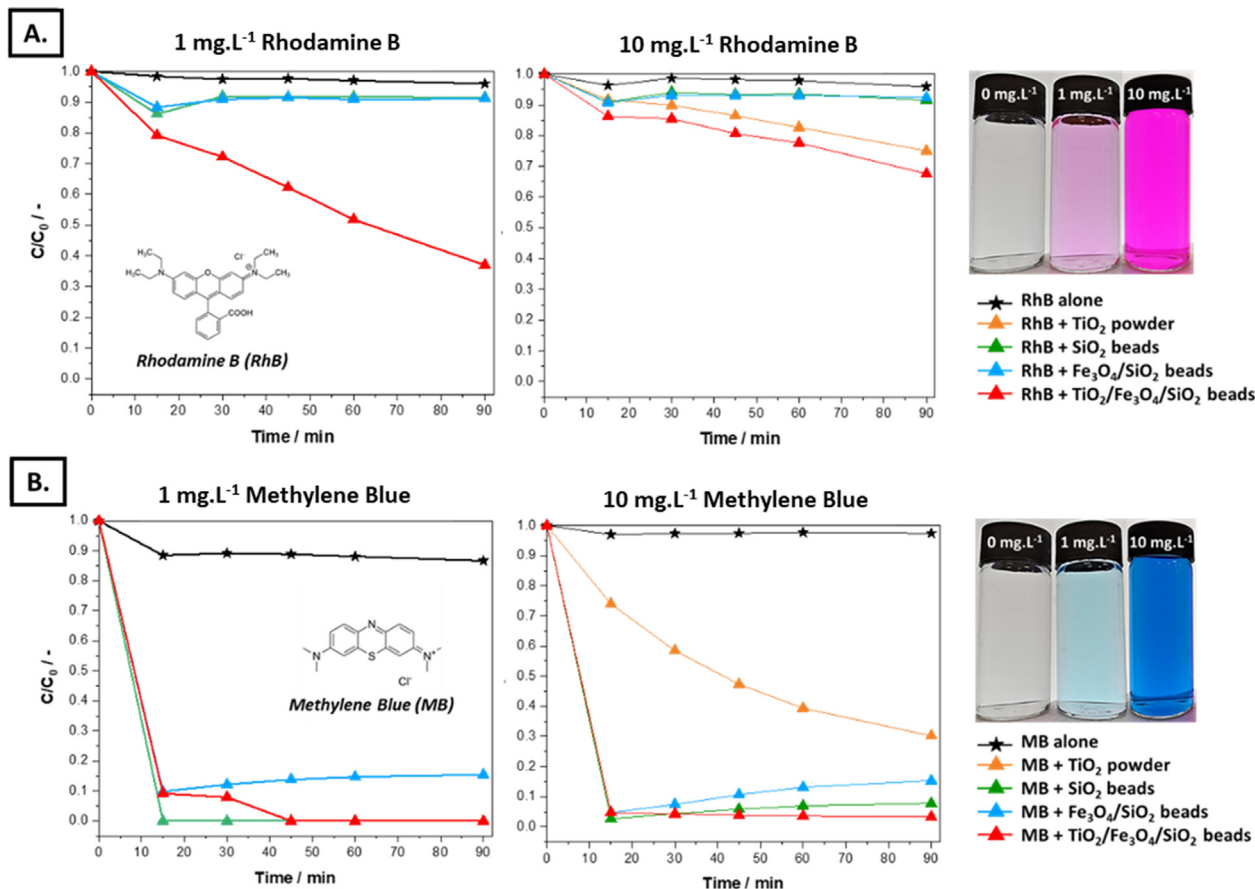


Fig. 4. Photodegradation under UV-light of (A) Rhodamine B and (B) Methylene Blue solutions (50 mL, 1 or 10 $\text{mg}\cdot\text{L}^{-1}$) in the presence of either TiO_2 powder (2.5 mg) or SiO_2 , $\text{Fe}_3\text{O}_4/\text{SiO}_2$ or $\text{TiO}_2/\text{Fe}_3\text{O}_4/\text{SiO}_2$ beads (20 mg). (For interpretation of the references to colour in this figure legend, the reader is referred to the web version of this article.)

loidal destabilization. The second possibility is that incorporation of oil into the bead structure results in an expansion of the beads. Given the apparent changes in porosity with higher concentrations of Span 80, this explanation seems more feasible. The substantial decrease of the beads' diameter with 2 wt% Span 80 is likely to be due to the fragmentation of the beads during separation as a result of higher fragility from the increased porosity. Additional optical microscopy images, EDX analysis as well as size distribution histograms of the beads with various concentrations of Span 80 are given in **Figs. S3–S6**.

Particle reproducibility was assessed by producing multiple batches. The beads were similar in both size and morphology with preparation yields between 60 and 81% (**Table 1**). Electrophoretic mobility measurements carried out at pH 7 indicate that the beads were negatively charged. Electrophoretic mobility values are displayed in **Table 1**, instead of zeta potential, due to the non-spherical nature of some beads. The mobility values obtained correspond to spherical particles with zeta potentials between -16 and -21 mV, explaining the stability as well as adsorption properties of the beads.

3.2. Photocatalytic degradation

3.2.1. Simple dye removal

Rhodamine B solutions showed stability under both visible and UV-light with a degradation of less than 4% after 90 min of irradiation (**Fig. 4A** and **Fig. S7A**). A slight increase in dye removal was observed in the presence of SiO_2 and $\text{Fe}_3\text{O}_4/\text{SiO}_2$ beads with values up to 9%. The absence of TiO_2 in the structure as well as the similar results obtained under both visible and UV-light suggest this increase is due to adsorption of dye on bead surfaces and not photodegradation. A significant increase in dye removal was observed in the presence of $\text{TiO}_2/\text{Fe}_3\text{O}_4/\text{SiO}_2$ beads. After 90 min of UV-light, 63% of 1 mg L^{-1} and 32% of 10 mg L^{-1} Rhodamine B was removed from solution. The large difference with the results under visible light (**Fig. S7A**) confirms this removal to be due to photodegradation and highlights the need for UV light in the photodegradation process. Solutions composed only of 10 mg L^{-1} of Rhodamine B and 2.5 mg of TiO_2 nanoparticles, showed a degradation of 25%, confirming superior results obtained with $\text{TiO}_2/\text{Fe}_3\text{O}_4/\text{SiO}_2$ beads.

Methylene Blue solutions exhibited stability under both visible and UV-light with degradation between 5 and 10% after 90 min of irradiation (**Fig. 4B** and **Fig. S7B**). A large increase in dye removal was observed with SiO_2 beads, with 100% removal from 1 mg L^{-1} solution and 92% from 10 mg L^{-1} solution. For $\text{Fe}_3\text{O}_4/\text{SiO}_2$ beads, 85% removal was observed for both 1 mg L^{-1} and 10 mg L^{-1} solutions. The similar results obtained under visible light (**Fig. S7B**) suggest adsorption of the dye on the beads rather than degradation. The greater adsorption with SiO_2 beads is likely to be due to their smaller diameter, offering a larger surface area and stronger attractive interactions with Methylene Blue due to opposing charges. Between 97 and 100% of the dye was removed from solution in the presence of $\text{TiO}_2/\text{Fe}_3\text{O}_4/\text{SiO}_2$ beads. Comparison with visible light experiments (**Fig. S7B**) suggests a process composed of both adsorption and photodegradation, enabling complete removal of Methylene Blue. The reference solution, composed of 10 mg L^{-1} of Methylene Blue and 2.5 mg of TiO_2 nanoparticles showed 70% degradation, confirming improved results obtained with $\text{TiO}_2/\text{Fe}_3\text{O}_4/\text{SiO}_2$ beads.

3.2.2. Optimization of photodegradation conditions

Optimization experiments focused on the effect of bead structure and load on photodegradation of Rhodamine B in water.

Modifying the porosity using Span 80 enables an increase in the photodegradation efficiency from 3 to 7% (**Fig. 5A**). Unexpectedly, greater dye removal was observed for beads prepared with

0.5 wt% Span 80, showing a degradation percentage of 39% after 90 min of UV-light irradiation. We believe the smaller improvement of degradation observed for beads prepared with higher amounts of Span 80 to be due to their larger diameter, which reduces their total number and thus surface area in solution or to the presence of residual Span 80 on the beads impeding access of dye to the photocatalyst.

Using higher bead loadings (60 mg instead of 20 mg) appears to have a significant effect, increasing photodegradation efficiency by 14%, thus enabling 53% of Rhodamine B to be degraded after 90 min of treatment (**Fig. 5A**). Higher bead loadings increase the total amount of photocatalyst accessible in solution. However, the photodegradation efficiency is also limited by the number of photons supplied to the system. The small difference observed between degradation in the presence of 40 and 60 mg of beads suggests that UV-light penetration is a limiting factor. Longer degradation experiments confirmed this hypothesis, showing increases in dye removal with longer exposure times (**Fig. 5B**).

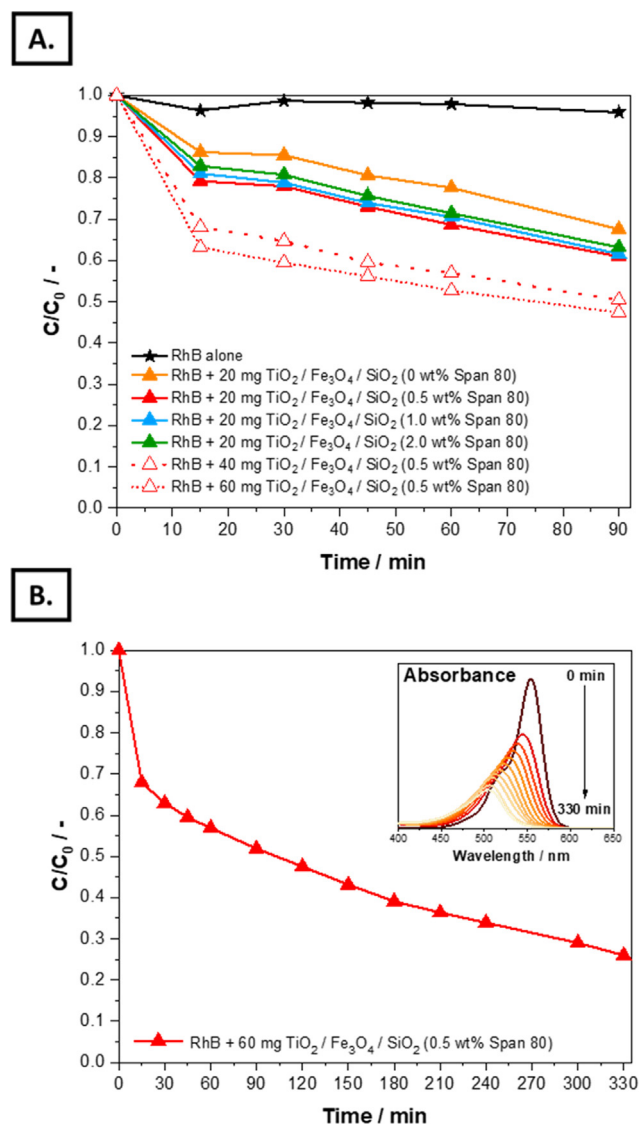


Fig. 5. Optimization of UV-light induced photodegradation of Rhodamine B solutions (50 mL , 10 mg L^{-1}) in the presence of $\text{TiO}_2/\text{Fe}_3\text{O}_4/\text{SiO}_2$ beads. Impact of (A) Beads' morphology & load and (B) UV-light exposure.

3.2.3. Recycling tests

The reusability of $\text{TiO}_2/\text{Fe}_3\text{O}_4/\text{SiO}_2$ beads for removal of Rhodamine B and Methylene Blue in water was also investigated following magnetic recovery of the beads (Fig. 6).

Experiments carried out with Rhodamine B solutions showed a significant improvement in degradation efficiency, increasing from 50% after the first cycle to more than 95% in subsequent cycles (Fig. 6A). Optical microscopy images taken after recycling and presented in Fig. S8 do not show any change in the beads' structure. This observation negates the idea of bead fractionation enabling greater accessibility to the photocatalyst. Instead, these results may be due to removal of residual Span 80 from the structure, enabling better access of the dye via the pores and bead surfaces, and as such, the photocatalyst. Comparison of degradation obtained using only TiO_2 nanoparticles showed marked improvements for the $\text{TiO}_2/\text{Fe}_3\text{O}_4/\text{SiO}_2$ beads, with a degradation efficiency up to 2.5 times higher as well as the possibility to easily recover and reuse the beads.

Experiments carried out with Methylene Blue showed a high dye removal for the first three cycles with removal values above 90% obtained in the first 15 min of treatment (Fig. 6B). A decrease of efficiency is then observed during the fourth cycle at only 71%. This is likely to be due to saturation of the beads' surface with Methylene Blue during the earlier cycles, resulting in a decreased

capacity for adsorption. This idea is supported by the additional experiment at lower bead loading (20 mg) presented in Fig. S9, where the decrease of efficiency is even more pronounced with removal of only 30% of dye during the fourth cycle, suggesting a larger saturation of the bead surface. However, comparison with the degradation obtained with TiO_2 nanoparticles again showed significant improvements for $\text{TiO}_2/\text{Fe}_3\text{O}_4/\text{SiO}_2$ beads, which can be used for three consecutive treatment cycles with higher treatment efficiency.

3.2.4. Mixtures of Rhodamine B / Methylene Blue

Removal efficiency from treatment of Rhodamine B and Methylene Blue mixtures with $\text{TiO}_2/\text{Fe}_3\text{O}_4/\text{SiO}_2$ beads are presented in Fig. 7. Absorption spectra obtained for the different cycles are presented in Figs. S10 and S11.

Methylene Blue was easily removed from solution for the two concentrations investigated. For Rhodamine B, an increase of the degradation efficiency was observed after recycling. This is consistent with the unmixed dye results and is likely to be due to the removal of Span 80 from the beads. The decrease of efficiency observed after four cycles in 5 mg L^{-1} dye mixtures is likely to be due to partial saturation of the beads' surface with Methylene Blue. This saturation hinders accessibility to the photocatalyst. However, comparison with the reference system still showed

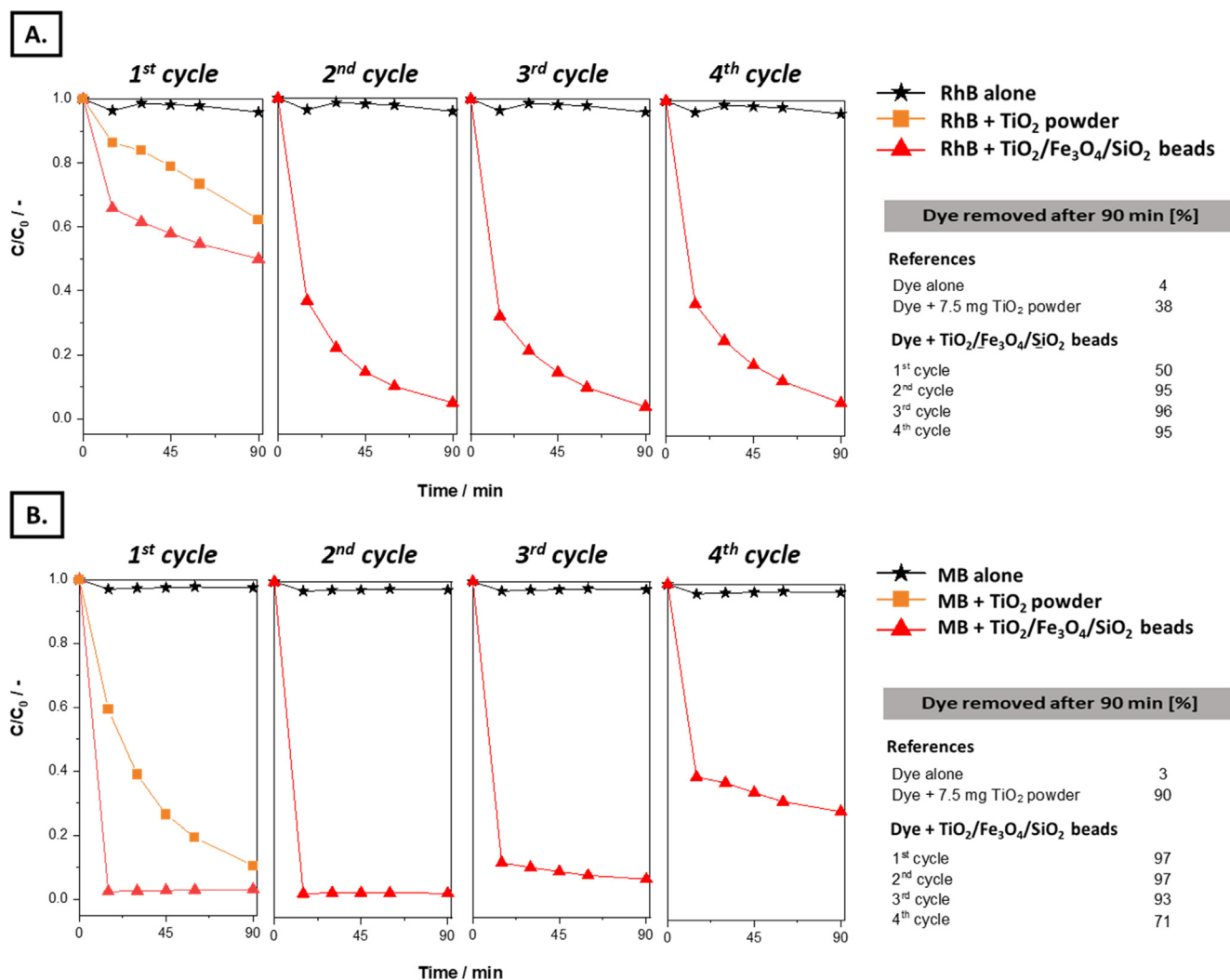


Fig. 6. Reusability of $\text{TiO}_2/\text{Fe}_3\text{O}_4/\text{SiO}_2$ (0.5% Span 80) beads (60 mg) after consecutive treatments of (A) Rhodamine B and (B) Methylene Blue solutions (50 mL, 10 mg L^{-1}) under UV-light. (For interpretation of the references to colour in this figure legend, the reader is referred to the web version of this article.)

improved results for $\text{TiO}_2/\text{Fe}_3\text{O}_4/\text{SiO}_2$ beads in the treatment of Rhodamine B and Methylene Blue mixtures. Therefore, this system can simultaneously remove both dyes from solution and easily be recovered with a magnet for reuse in another solution.

3.2.5. Suggested mechanism for dye removal

Removal of Rhodamine B is based on photodegradation, induced by the presence of TiO_2 . This is a well-known UV light-induced photoexcitation process, where electrons are transferred from a valence band to a conduction band. The electron and hole pair generated react with O_2 and H_2O to subsequently form superoxide species (O_2^-) and hydroxyl radicals (OH^\cdot), which are then involved in oxidation of the dye and its final mineralization into CO_2 and water. [4,6,13,18,45] Results presented in Fig. S12 suggest different photodegradation processes in the presence of TiO_2 nanoparticles versus $\text{TiO}_2/\text{Fe}_3\text{O}_4/\text{SiO}_2$ beads. With TiO_2 nanoparticles, a gradual decrease of the maximum absorption is observed over time with no peak shift. In the presence of the beads, both a decrease in absorbance and a hypsochromic shift are observed. The decrease in absorbance is likely due to degradation of the aromatic structure within the organic dye by in situ generated radicals. [46–48] The hypsochromic shift is due to the de-ethylation of Rhodamine B. [46–48] Continual shifting towards shorter wavelengths was observed for longer photodegradation times (Fig. 5B inset), with no further shifting observed after 6 h of exposure, leading to a peak around 500 nm. This value is consistent with the 498 nm Rhodamine peak [47] reported in literature, which supports the idea of de-ethylation of Rhodamine B. Guo *et al.* suggested this is more likely to happen for systems with stronger adsorption properties, [48] which supports the occurrence with $\text{TiO}_2/\text{Fe}_3\text{O}_4/\text{SiO}_2$ beads and not TiO_2 nanoparticles. The difference of absorbance between Rhodamine B and Rhodamine is small [46,47], but we can conclude Rhodamine B undergoes a simultaneous degradation of its conjugated xanthene ring and a de-ethylation process generating Rhodamine, which is subsequently degraded over time.

Removal of Methylene Blue appears to be due to both adsorption onto the silica surface and photodegradation. The sudden decrease in absorbance observed in the presence of the beads under both visible and UV-light, suggests the adsorption mechanism to be dominant, at least initially. Photodegradation, characterized by a steady decrease in absorbance over time, appears to be significant only after partial saturation of the beads surface as suggested with the change of slope shown in Fig. 6 and S9.

The difference of adsorption between Rhodamine B and Methylene Blue in the presence of $\text{TiO}_2/\text{Fe}_3\text{O}_4/\text{SiO}_2$ beads, is likely based on the overall charge of the two molecules. As shown in Fig. 4B inset, Methylene Blue is a cationic compound with no functional groups that are susceptible to changes in pH. Hence, adsorption on the beads is favoured due to charge-based attraction. On the contrary, Rhodamine B features a carboxylic acid group in its structure in addition to the quaternary ammonium (Fig. 4A inset). The pK_a of the carboxylic acid group is approximately 4, implying that at neutral pH (experimental conditions) a significant proportion of these groups will be deprotonated, conferring a neutral charge to the dye. As such, adsorption on the beads due to charge-based attraction will be minimized for Rhodamine B.

The presence of negative charges on the beads was shown to enhance the removal of positively charged dyes from solution via adsorption. However, such surface charges can also establish a limit for removal of negatively charged dyes. Allura red AC, from the azo dye class, was used as an anionic dye molecule to investigate this prospect. A preliminary study, shown in Fig. S13, demonstrates only 9% degradation of a 10 mg L^{-1} Allura red AC solution (50 mL) after 90 min of UV-light irradiation in the presence of 60 mg of beads prepared with 0.5% Span 80. The complete degra-

ation of the dye observed with 7.5 mg TiO_2 powder confirmed the ability of TiO_2 nanoparticles to photodegrade Allura red AC under UV-light. The low degradation observed in the presence of the beads is likely to be due to electrostatic repulsions: both beads and dye are negatively charged, making access to the photocatalyst improbable. Future work will address this limitation by investigating the effects of pH as well as addition of electrolytes in solution to facilitate interactions between the photocatalyst and negatively charged species [16].

The need for UV-light to achieve the photodegradation resides in the large band gap for TiO_2 , which is estimated at 3.2 eV [16,45]. Consequently, TiO_2 requires an excitation wavelength below 400 nm. UV-light represents only 3–5% of solar light [16,45], which may limit use of $\text{TiO}_2/\text{Fe}_3\text{O}_4/\text{SiO}_2$ beads in certain

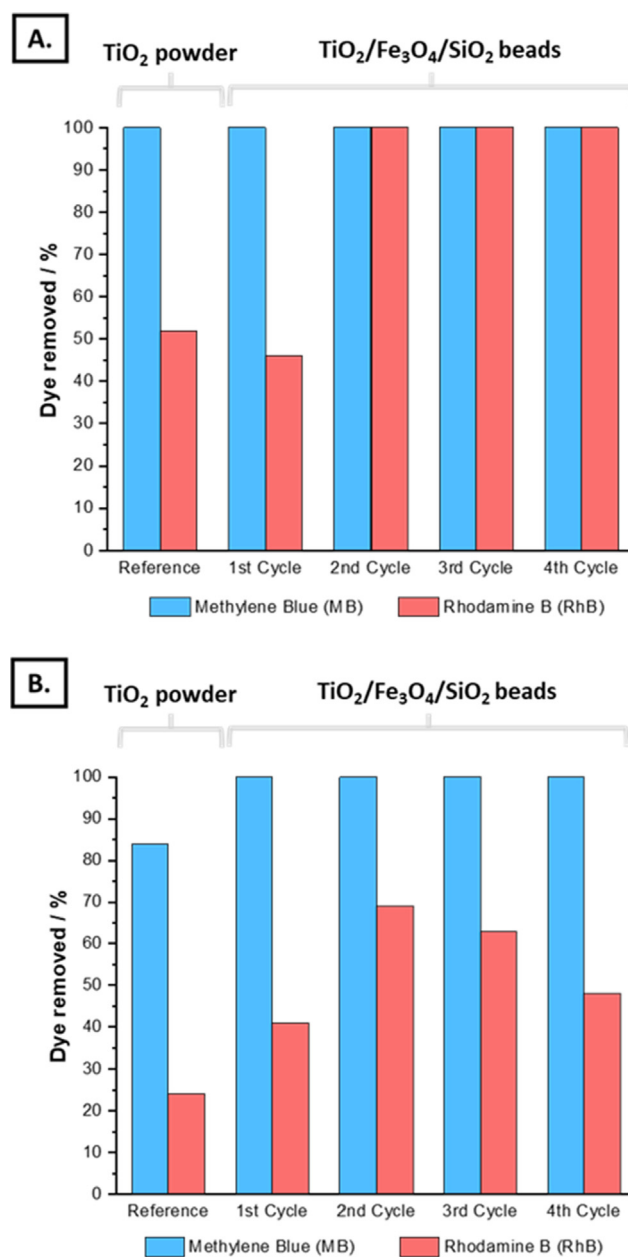


Fig. 7. Reusability of $\text{TiO}_2/\text{Fe}_3\text{O}_4/\text{SiO}_2$ (0.5% Span 80) beads (60 mg) after consecutive treatments of mixtures of Rhodamine B and Methylene Blue (50 mL, (A) 1 mg L^{-1} or (B) 5 mg L^{-1} of each dye) under UV-light irradiation (90 min). (For interpretation of the references to colour in this figure legend, the reader is referred to the web version of this article.)

applications. To address this issue, metal and non-metal TiO₂ doping have been reported to decrease the band gap, enabling photodegradation under visible light [5,10,45,49–51]. Future work will assess whether the incorporation of additional metal oxide nanoparticles to the beads structure may lead to similar results.

4. Conclusion

Micron-sized TiO₂/Fe₃O₄/SiO₂ photocatalysts were prepared at room temperature via salt-driven assembly of commercial nanoparticles in reverse emulsion droplets. This production method relies on charge screening by CaCl₂ addition which reduces stabilising repulsive forces between particles resulting in their irreversible agglomeration into spherical beads. The incorporation of various metal oxides nanoparticles (TiO₂, Fe₃O₄ and SiO₂) to the structure enables to imbue the final agglomerates with magnetic responsiveness as well as adsorption and photodegradation properties as highlighted by the removal of Rhodamine B and Methylene Blue from solution under UV-irradiation. Morphology of beads were easily tuned by addition of a hydrophobic surfactant, Span 80, to the oil phase. It is believed the presence of surfactant resulted in incorporation of oil to the beads structure which subsequently generated holes and cavities after cleaning, thus offering a green approach for producing porous materials.

The degradation efficiency of Rhodamine B was directly correlated to the beads' morphology and loading, initial dye concentration and external light intensity. Reusability of the beads was confirmed, showing a dye removal efficiency in optimized conditions (60 mg of TiO₂/Fe₃O₄/SiO₂ – 0.5% Span, 50 mL of 10 mg L⁻¹ dye solution) greater than 93% per cycle for three consecutive cycles; 90% of Methylene Blue and Rhodamine B removed during the first 15 and 45 min of treatment. Photodegradation experiments carried out in the presence of a mixture of Rhodamine B and Methylene Blue confirmed that both dyes could be simultaneously removed, with Rhodamine B being photodegraded and Methylene Blue being mostly adsorbed.

This method appears as a fast and cheap alternative for producing micron-sized magnetic photocatalysts from commercial nanoparticles without expensive equipment, toxic chemicals or high temperatures as reported in previous studies. [22–35] Furthermore, the presence of both silica and titania on the surface differs from usual core-shell structure, [5,22–35] paving the way to further potential surface functionalization of the beads. Therefore, this work establishes a significant advance in composite materials, offering a green, tuneable and easy to implement single preparation method.

CRedit authorship contribution statement

David F.F. Brossault: Conceptualization, Methodology, Validation, Investigation, Writing - original draft, Visualization. **Thomas M. McCoy:** Conceptualization, Resources, Writing - review & editing. **Alexander F. Routh:** Conceptualization, Methodology, Resources, Writing - review & editing, Supervision, Project administration, Funding acquisition.

Declaration of Competing Interest

The authors declare that they have no known competing financial interests or personal relationships that could have appeared to influence the work reported in this paper.

Acknowledgements

The authors thank Dr Heather Greer from the department of Chemistry (University of Cambridge) for helping with the imaging characterizations (SEM, STEM and EDX analysis). D.F.F Brossault thanks the University of Cambridge for funding through a WD Armstrong PhD scholarship.

Appendix A. Supplementary material

Supplementary data to this article can be found online at <https://doi.org/10.1016/j.jcis.2020.10.001>.

References

- [1] C. Xu, P.R. Anusuyadevi, C. Aymonier, R. Luque, S. Marre, *Chem. Soc. Rev.* 48 (2019) 3868–3902.
- [2] V. Polshettivar, R. Luque, A. Fihri, H. Zhu, M. Bouhrara, J.M. Basset, *Chem. Rev.* 111 (2011) 3036–3075.
- [3] M.J. Jacinto, L.F. Ferreira, V.C. Silva, *J. Sol-Gel. Sci. Technol.* 96 (2020) 1–14.
- [4] S.Q. Liu, *Environ. Chem. Lett.* 10 (2012) 209–216.
- [5] H. Yao, M. Fan, Y. Wang, G. Luo, W. Fei, *J. Mater. Chem. A* 3 (2015) 17511–17525.
- [6] Y.L. Pang, S. Lim, H.C. Ong, W.T. Chong, *Ceram. Int.* 42 (2016) 9–34.
- [7] A. Akhundi, A. Habibi-Yangjeh, M. Abitorabi, A.R. Pouran, *Catal. Rev.* 61 (4) (2018) 595–628.
- [8] A. Akhundi, A. Badiei, G.M. Ziarani, A. Habibi-Yangjeh, M.J. Munoz-Batista, R. Luque, *J. Mol. Catal. B Enzym.* 488 (2020) 110902.
- [9] N. Ahmadpour, M.H. Sayadi, S. Sobhani, M. Hjjani, *J. Environ. Manage.* 271 (2020) 110964–110975.
- [10] A. Kumar, M. Khan, L. Fang, I.M.C. Lo, *J. Hazard. Mater.* 370 (2019) 108–116.
- [11] X. Xie, Y. Liu, X. Dong, C. Lin, X. Wen, Q. Yan, *Appl. Surf. Sci.* 450 (2018) 742–747.
- [12] S. Li, Z. Wang, X. Zhao, X. Yang, G. Liang, X. Xie, *Chem. Eng. J.* 360 (2019) 600–611.
- [13] R. Gousain, K. Gupta, P. Joshi, O.P. Khatri, *Adv. Colloid Interface Sci.* 272 (2019) 102009–102033.
- [14] V. Belessi, D. Lambropoulou, I. Konstantinou, R. Zboril, J. Tucek, D. Jancik, T. Albanis, D. Petridis, *Appl. Catal. B* 87 (3–4) (2009) 181–189.
- [15] A. Habibi-Yangjeh, S. Asadzadeh-Khaneghah, S. Feizpoor, A. Rouhi, *J. Colloid Interf. Sci.* 580 (2020) 503–514.
- [16] A. Ajmal, I. Majeed, R.N. Malik, H. Idriss, M.A. Nadeem, *RSC Adv.* 4 (2014) 37003–37026.
- [17] V. Katheresan, J. Kandedo, S.Y. Lau, *J. Environ. Chem. Eng.* 6 (4) (2018) 4676–4697.
- [18] A.H.S. Chan, T.Y. Wu, J.C. Juan, C.Y. Teh, *J. Chem. Technol. Biotechnol.* 86 (9) (2011) 1130–1158.
- [19] S.W. Lee, J. Drwiega, D. Mazyck, C.Y. Wu, W.M. Sigmund, *Mater. Chem. Phys.* 96 (2006) 483–488.
- [20] M. Pirhashemi, A. Habibi-Yangjeh, S.R. Pouran, *J. Ind. Eng. Chem.* 62 (2018) 1–25.
- [21] M. Shekofteh-Gohari, A. Habibi-Yangjeh, M. Abitorabi, A. Rouhi, *Crit. Rev. Environ. Sci. Technol.* 48 (10–12) (2018) 806–857.
- [22] S. Watson, D. Beydoun, R. Amal, *J. Photoch. Photobio. A* 148 (1–3) (2002) 303–313.
- [23] P. Arora, A. Fermah, J.K. Rajput, H. Singh, J. Badhan, *Environ. Sci. Pollut. Res. Int.* 24 (2017) 19546–19560.
- [24] C.F. Chang, C.Y. Man, *Ind. Eng. Chem. Res.* 50 (2011) 11620–11627.
- [25] J. Su, Y. Zhang, S. Xu, S. Wang, H. Ding, S. Pan, G. Wang, G. Li, H. Zhao, *Nanoscale* 6 (2014) 5181–5192.
- [26] W. Wu, X. Xiao, S. Zhang, F. Ren, C. Jiang, *Nanoscale Res. Lett.* 6 (2011) 533–548.
- [27] L. Zhang, Z. Wu, L. Chen, L. Zhang, X. Li, H. Xu, H. Wang, G. Zhu, *Solid State Sci.* 52 (2016) 42–48.
- [28] C. Liu, Y. Li, Q. Duan, *Appl. Surf. Sci.* 503 (2020) 14111–141123.
- [29] J. Chang, Q. Zhang, Y. Liu, Y. Shi, Zhao. Qin, *J. Mater. Sci.: Mater. Electron* 29 (2018) 8258–8266.
- [30] S. Salamat, H. Younesi, N. Bahramifar, *RSC Adv.* 7 (2017) 19391–19405.
- [31] Z. Lenzion-Bielun, A. Wojciechowska, J. Grzechulska-Damszel, U. Narkiewicz, Z. Sniadecki, B. Idzikowski, *J. Phys. Chem. Solids* 136 (2020) 109178–109184.
- [32] Z. Bielan, A. Sulowska, S. Dudziak, K. Siuzdak, J. Ryl, A. Zielinska-Jurek, *Catalysts* 10 (2020) 672–692.
- [33] K.H. Choi, S.Y. Park, B.J. Park, J.S. Jung, *Surf. Coat. Technol.* 320 (2017) 240–245.
- [34] T.A. Gad-Allah, K. Fujimura, S. Kato, S. Satawata, T. Kojima, *J. Hazard. Mater.* 154 (2008) 572–577.
- [35] Y. Wang, F. Pan, W. Dong, L. Xu, K. Wu, G. Xu, W. Chen, *Appl. Catal. B* 189 (2016) 192–198.
- [36] S.H. Dewi, S.A. Fisli, S. Wardiyati, *J. Phys.: Conf. Ser.* 739 (2016) 012113–012121.
- [37] A.L. Costa, B. Ballarin, A. Spegni, F. Casoli, D. Gardini, *J. Colloid Interf. Sci.* 388 (1) (2012) 31–39.

- [38] A. Zielinska-Jurek, Z. Bielan, I. Wysocka, J. Strychalska, M. Janczarek, T. Klimczuk, *J. Environ. Manage.* 195 (2017) 157–165.
- [39] D.F.F. Brossault, A.F. Routh, *J. Colloid Interf. Sci.* 562 (2020) 381–390.
- [40] J. Kim, J.E. Lee, J. Lee, J.H. Yu, B.C. Kim, K. An, Y. Hwang, C.H. Shin, J.G. Park, J. Kim, T. Hyeon, *J. Am. Chem. Soc.* 128 (3) (2006) 688–689.
- [41] Y. Zhu, T. Ikoma, N. Hanagata, S. Kaskel, *Small* 6 (3) (2010) 471–478.
- [42] J. Kim, H.S. Kim, N. Lee, T. Kim, H. Kim, T. Yu, I.C. Song, W.K. Moon, T. Hyeon, *Angew. Chem.* 120 (44) (2008) 8566–8569.
- [43] F. Gao, X. Wu, D. Wu, J. Yu, J. Yao, Q. Qi, Z. Cao, Q. Cui, Y. Mi, *Colloids Surf. A Physicochem. Eng. Asp.* 587 (2020) 124363–124374.
- [44] J. Yao, F. Gao, X. Liang, Y. Li, Y. Mi, Q. Qi, J. Yao, Z. Cao, *Colloids Surf. A Physicochem. Eng. Asp.* 570 (2019) 449–461.
- [45] H. Kisch, W. Macyk, *Chemphyschem* 3 (2002) 399–400.
- [46] Y. Ma, J. Yao, *J. Photochem. Photobiol. A* 116 (2) (1998) 167–170.
- [47] T. Watanabe, T. Takizama, K. Honda, *J. Phys. Chem.* 81 (19) (1977) 1845–1851.
- [48] C. Guo, J. Xu, Y. He, Y. Zhang, Y. Wang, *Appl. Surf. Sci.* 257 (8) (2011) 3798–3803.
- [49] A. Suligoj, I. Arcon, M. Mazaj, G. Frazic, D. Arcon, P. Cool, U.L. Stangar, N.N. Tusar, *J. Mater. Chem. A* 6 (2018) 9882–9892.
- [50] J. Wang, S. Uma, K.J. Klabunde, *Appl. Catal. B* 48 (2004) 151–154.
- [51] K. Wilke, H.D. Breuer, *J. Photochem. Photobiol. A* 121 (1999) 49–53.